# An Efficient Pan-Sharpening Method via a Combined Adaptive PCA Approach and Contourlets

Vijay P. Shah, *Member, IEEE*, Nicolas H. Younan, *Senior Member, IEEE*, and Roger L. King, *Senior Member, IEEE*

***Abstract*—High correlation among the neighboring pixels both spatially and spectrally in a multispectral image makes it necessary to use an efficient data transformation approach before performing pan-sharpening. Wavelets and principal component analysis (PCA) methods have been a popular choice for spatial and spectral transformations, respectively. Current PCA-based pan-sharpening methods make an assumption that the first principal component (PC) of high variance is an ideal choice for replacing or injecting it with high spatial details from the high-resolution histogram-matched panchromatic (PAN) image. This paper presents a combined adaptive PCA–contourlet approach for pan-sharpening, where the adaptive PCA is used to reduce the spectral distortion and the use of nonsubsampled contourlets for spatial transformation in pan-sharpening is incorporated to overcome the limitation of the wavelets in representing the directional information efficiently and capturing intrinsic geometrical structures of the objects. The efficiency of the presented method is tested by performing pan-sharpening of the high-resolution (IKONOS and QuickBird) and the medium-resolution (Landsat-7 Enhanced Thematic Mapper Plus) datasets. The evaluation of the pan-sharpened images using global validation indexes reveal that the adaptive PCA approach helps reducing the spectral distortion, and its merger with contourlets provides better fusion results.**

***Index Terms*—Contourlets, image fusion, pan-sharpening, principal component analysis (PCA), wavelets.**

## I. Introduction

THE DESIGN of optical sensors allows the selection of any two of the following three parameters—spatial resolution, spectral resolution, and signal-to-noise ratio (SNR). The spectral and spatial resolutions have an inverse relationship [1]. Thus, a high spectral resolution results in a low spatial resolution and vice versa. High spatial and spectral resolutions are necessary to perform various complex tasks in urban and land–cover classifications [2]. The injection of fine spatial information from the high spatial resolution panchromatic (PAN) image into the low spatial resolution multispectral (MS) images to get high spatial resolution MS images is known as pan-sharpening. Pan-sharpening has been an active area of research for more than a decade, and many pan-sharpening methods have been proposed [2]–[6]. Pan-sharpening using the complementary information from the MS and PAN Images is gaining popularity because it helps to reduce spectral distortion by increasing spatial resolution. In the past few years, several pan-sharpening methods using multiresolution approaches of discrete wavelet transform [7], [8], Laplacian pyramid [9], and à trous wavelet transform [10] are proposed, where the detail spatial information from the PAN image is injected in the multispectral image. Properties, such as multiresolution, localization, critical sampling, and limited directionality (horizontal, vertical, and diagonal directions), have made the wavelet transform a popular choice for feature extraction, image denoising, and pan-sharpening [2], [11]. However, wavelets fail to capture the smoothness along the contours [11].

An efficient representation of the image should ideally possess properties of multiresolution, localization, critical sampling, directionality, and anisotropy [11], [12]. The contourlet transform, an alternative multiresolution approach, provides an efficient directional representation and is also efficient in capturing intrinsic geometrical structures of the natural image along the smooth contours [11]. Remote sensing images have presence of natural and man-made objects, e.g., rivers, roads, coastal areas, buildings, etc., which indicate higher geometrical content. Thus, transformations, taking into consideration the geometric structure along with other properties of wavelet transformation, will be more useful for image fusion or pan-sharpening. Recently, contourlets have been used for image fusion of optical and synthetic aperture radar imagery [13], [14].

High correlation among the spectral bands has lead to using the intensity–hue–saturation (IHS) transformation or principal component analysis (PCA) transformation along the spectral axis [2]. The PCA-based method has been popularly used for spectral transformation because the first principal component (PC1) consists of the most variance, making it a suitable choice to replace the PAN component [15]. However, this method provides more spectral artifacts for images consisting of vegetation. To overcome this problem, Gonzalez–Audicana *et al.* proposed a pan-sharpening method based on a merger of a wavelet–PCA method where only the details of PC1 are replaced by the details of the PAN image [2]. However, such a standard approach of replacing the first PC is not based on any statistics between the high-resolution PAN image and the low-resolution first PC image. A higher variance of the first PC does not necessarily mean it has higher correlation with the PAN image. Thus, the replacement of the first PC may not always be a suitable choice.

In this paper, a combined adaptive PCA–contourlet method is developed to improve the PCA-based image fusion method

Manuscript received June 6, 2007; revised October 5, 2007.

V. P. Shah was with the Department of Electrical and Computer Engineering and the GeoResources Institute, Mississippi State University, Mississippi State, MS 39762 USA. He is now with SAIC-Frederick, Inc., National Cancer Institute (National Institutes of Health), Bethesda, MD 20814 USA (e-mail: vijaypshah@yahoo.com).

N. H. Younan and R. L. King are with the Department of Electrical and Computer Engineering and the GeoResources Institute, Mississippi State University, Mississippi State, MS 39762 USA (e-mail: younan@ece.msstate.edu; rking@engr.msstate.edu).

Color versions of one or more of the figures in this paper are available online at http://ieeexplore.ieee.org.

Digital Object Identifier 10.1109/TGRS.2008.916211

by adaptively selecting the component for the substitution or injection of high spatial details, whereas the contourlet transform is used to improve the spatial transformation in the pan-sharpening process. High-resolution (IKONOS and QuickBird) and medium-resolution [Landsat-7 Enhanced Thematic Mapper Plus (ETM+)] imagery datasets, having high vegetation contents, are used to validate the applicability of the presented method, and the resulting pan-sharpened images are evaluated in terms of known global validation indexes.

This paper is organized as follows. Section II briefly reviews the standard PCA-based methods. Section III presents the methodology used to improve pan-sharpening. Experimental results and comparisons are provided in Section IV for different datasets. Conclusions are drawn in Section V.

## II. Review of PCA-Based Pan-Sharpening

This section briefly reviews the standard PCA-based component substitution method and the PCA–wavelet merger method.

### A. Standard PCA-Based Component Substitution

PCA is a commonly used technique for spectral transformation of the original data yielding uncorrelated principal components by a linear combination. In the PCA-based component substitution method, the first PC image is replaced by the PAN image [5]. Here, it is assumed that the first PC image with the largest variance contains the major information from the original image and hence would be an ideal choice to replace the high spatial resolution PAN image. The PAN image is histogram matched with the first PC before the substitution. The remaining PCs, considered to have band-specific information, are unaltered. Inverse PCA is performed on the modified PAN image and the PCs to obtain a high-resolution pan-sharpened image.

### B. PCA–Wavelet Merger Algorithm

The steps followed by the Gonzalez algorithm are [2] as follows.

- Apply PCA transformation to the MS image to obtain the PC1 image.
- Histogram match the PAN image to the PC1 image.
- Apply a subsampled or nonsubsampled wavelet transformation to the PC1 image and histogram matched the PAN image using an appropriate mother wavelet and for $N$ level of decomposition, where $N = \log_2$ (ratio of the PAN pixel size to the MS pixel size).
- Replace the detail wavelet coefficients of PC1 with the detail wavelet coefficients of the histogram-matched PAN image.
- Perform inverse wavelet transformation and inverse PCA transformation to obtain a high-resolution pan-sharpened image.

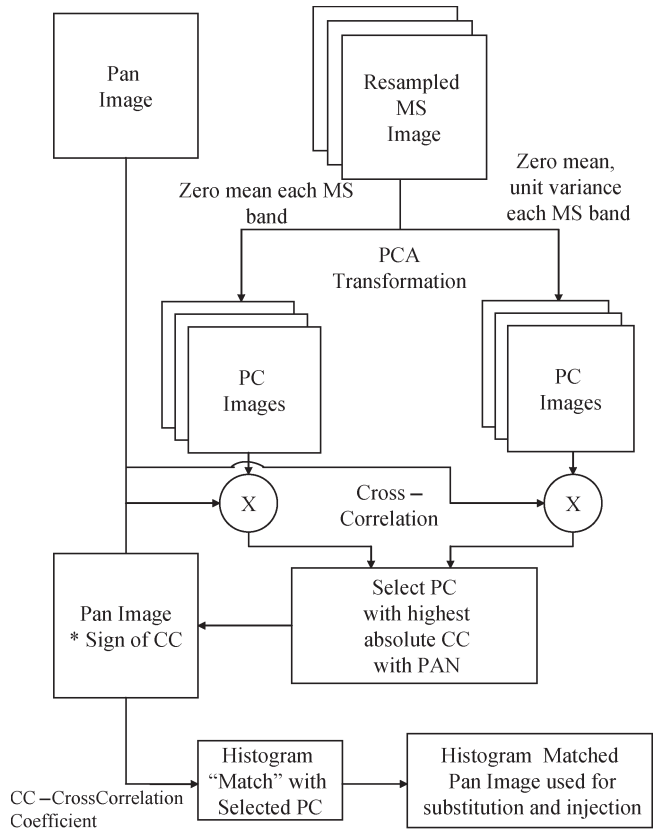


Fig. 1. Adaptive selection of PC for substitution and injection.

## III. Improved Adaptive PCA–Contourlet Merger Method

### A. Adaptive PCA Approach

PCA is a linear transformation of the multidimensional data. The data are transformed to a new coordinate system such that the first coordinate represents the largest variance (the first principal component) by any projection, the second coordinate to the second largest variance, and so forth. For more details, refer to [16]. Let $\mathbf{X}$ be a $p$-dimensional random column vector having a zero empirical mean. The PCA transformation tries to find an orthonormal projection $p \times p$ matrix $\mathbf{W}$ such that

$$\mathbf{s} = \mathbf{W^T X} \tag{1}$$

where the elements of $\mathbf{W}$ are the eigenvectors of the covariance matrix of $\mathbf{X}$.

Standard PCA-based pan-sharpening methods assume that the first PC having the highest variance has more information about the panchromatic image [17]. This substitution of component is not based on any statistical measure with the PAN image. Thus, it may not the best choice. To take into consideration the dependency between the PC's and the PAN images, a statistical measure, based on the cross-correlation coefficient, is incorporated into the process to adaptively determine the appropriate PC component that is to be substituted or injected with detail information. Since this process involves replacing the low-resolution spatial PC component with the highly correlated high spatial resolution PAN component, it is

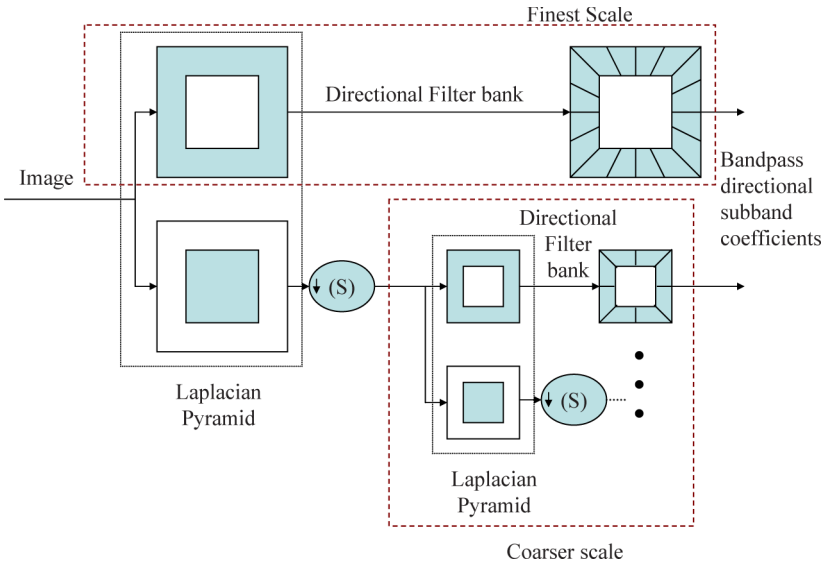


Fig. 2. Discrete contourlet transform. (This figure is a modified version of [11] and [12].)

expected that the newly adaptive PCA method will yield better results than the traditional one.

The similarity between images can be measured by the correlation coefficient. The value of the coefficient varies from $-1$ to 1, with a value close to $+1$ indicating a strong similarity between two images, whereas a value of $-1$ represents images not only with dissimilarity but also signifies that there is a strong inverse relationship between these two images. For a given two $N \times N$ pixels images, the cross-correlation coefficient is given by [18] as follows:

$$Corr(A|B) = \frac{\sum_{i=1}^{N}\sum_{j=1}^{N}(A_{i,j}-\bar{A})(B_{i,j}-\bar{B})}{\sqrt{\sum_{i=1}^{N}\sum_{j=1}^{N}(A_{i,j}-\bar{A})^2 \sum_{i=1}^{N}\sum_{j=1}^{N}(B_{i,j}-\bar{B})^2}}. \quad (2)$$

Fig. 1 shows a block diagram of the presented method. The steps involved in adaptively determining the appropriate PC component for substitution or details information injection are as follows.

- Perform standardization of the MS image using two different approaches.
  - Normalize each band to have zero mean and unit variance.
  - Normalize each band to have only zero mean.
- Perform PCA transformation on the standardized MS image.
- Calculate the cross-correlation coefficient (CC) between the PC's and the PAN image.
- Select the PC having the highest absolute value of the cross-correlation coefficient.
- Inverse the PAN image before performing histogram matching if the cross-correlation value is negative.
- Perform histogram matching of the selected PC and the PAN image.
- Use the histogram-matched PAN image in the PCA-based method for substitution or injection of the high spatial detail information.

It is worth mentioning that other normalization approaches to preprocess the data can be added to the system, which can affect the cross-correlation value. However, the overall system concept of the adaptive PCA remains unaffected. Furthermore, the two normalization approaches presented here are more general and cover a wider range.

### *B. Contourlet Transform*

Contourlets provide a new system representation for image analysis [11], [19]. The contourlet name is so called because of its ability to capture and link the point of discontinuities to form a linear structure (contours). The two-stage process used to derive the contourlet coefficients involves a multiscale transform and a local directional transform. The point of discontinuities and multiscale transformation is obtained via the Laplacian pyramid. The local directional filter bank is used to group these waveletlike coefficients to obtain a smooth contour. Contourlets provide $2l$ directions at each scale, where $l$ is the number of required orientation. This flexibility of having different numbers of direction at each scale makes contourlets different from other available multiscale and directional image representation [11], [12], [19]–[21], which includes 2-D Gabor wavelets [22], the cortex transforms [23], the steerable pyramid [24], 2-D directional wavelets [25], and brushlets [26]. Similar to wavelets, contourlets also have different implementation of the subsampled and nonsubsampled transforms.

*1) Discrete Contourlet Transform:* The discrete contourlet transform (CT) is developed in the discrete domain using the fast iterated nonseparable filter banks having an order of $N$ operations for $N$-pixel images [11]. The transformation stage includes two filter banks—the Laplacian pyramid to generate multiscale decomposition and the directional filter bank to reveal directional details at each decomposition level as illustrated in Fig. 2.

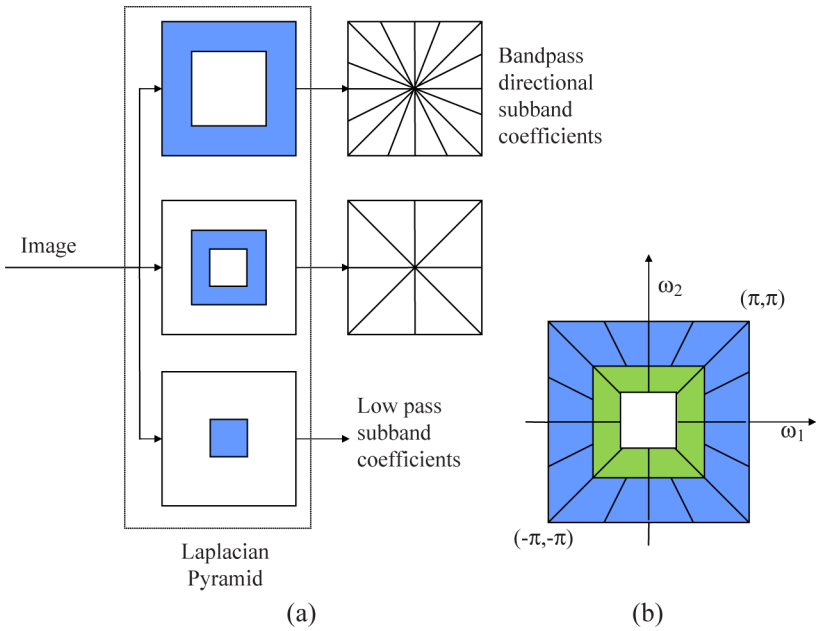


Fig. 3. Nonsubsampled contourlet transform. (a) Implementation of NSCT. (b) Frequency partitioning in idealized form. (This figure is a modified version of [11] and [12].)

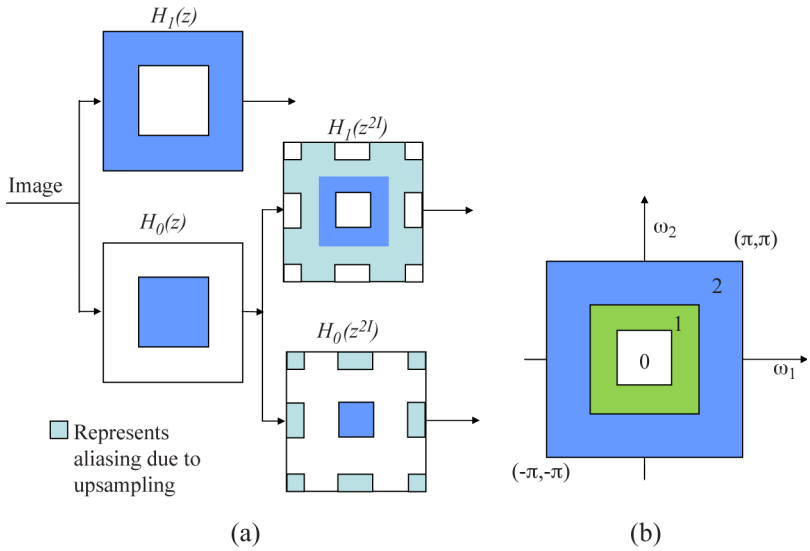


Fig. 4. Nonsubsampled pyramid. (a) Two-stage subband decomposition. (b) Frequency partitioning in idealized form. (This figure is a modified version of [11] and [12].)

The subsampled CT consists of downsampling the image by a factor of $M$ at each level of transformation. The 2-D filters are obtained from mapping 1-D filters. For perfect reconstruction, the 1-D filters satisfy the condition [21]

$$H_0(z)G_0(z) + H_1(z)G_1(z) = 2 \tag{3}$$

where $H_0(z)$ and $H_1(z)$ represent the low-pass and high-pass analysis filters, whereas $G_0(z)$ and $G_1(z)$ are the low-pass and high-pass synthesis filters. The 2-D perfect reconstruction is achieved by choosing the mapping filter $M(z)$ to satisfy the condition

$$H_0\left(M(\mathbf{z})\right)G_0\left(M(\mathbf{z})\right) + H_1\left(M(\mathbf{z})\right)G_1\left(M(\mathbf{z})\right) = 2. \tag{4}$$

$\boldsymbol{M}(z)$ has a separable property in the polyphase domain, which reduces the filter complexity from $\mathbf{O}(N^2)$ to $\mathbf{O}(N)$ [21].

The 2-D directional filter bank (DFB) is constructed in two steps. In the first step, the frequency spectrum is divided into horizontal and vertical directions using a two-channel quincunx filter bank [11], [27]. This is followed by the shearing operator. An appropriate choice of shearing operation and the two-direction partition of quincunx filter banks provide the required directional division of the 2-D spectrum. Similar to the discrete wavelet transform, the discrete contourlet transform is also shift variant. The nonsubsampled contourlet, which has slightly different filter design implementation, is shift invariant.

*2) Nonsubsampled Contourlet Transform (NSCT):* The NSCT with fast implementation provides a complete shift-invariant and multiscale representation, similar to the redundant

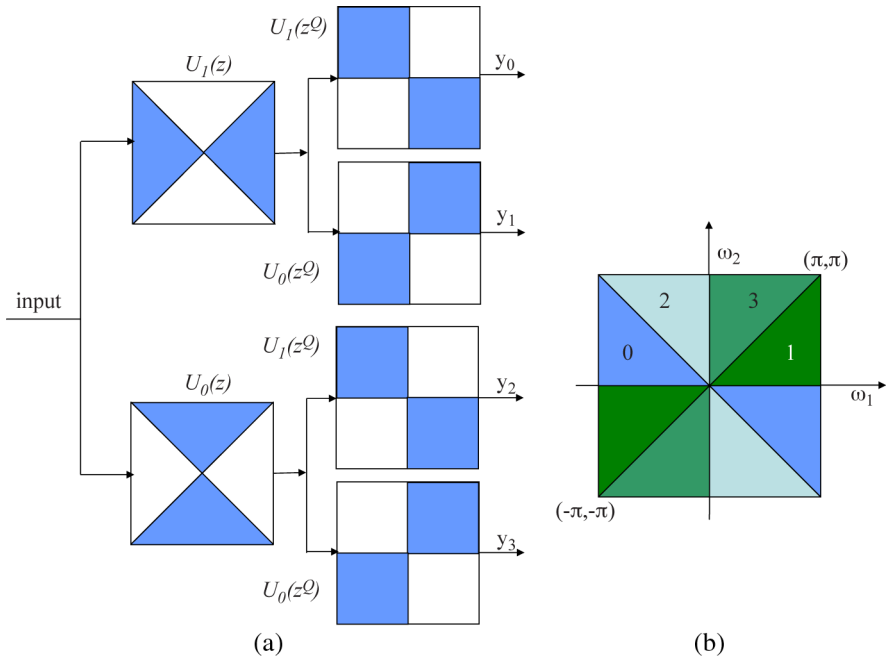


Fig. 5. Nonsubsampled directional filter banks. (a) Directional filter bank. (b) Directional frequency partitioning. (This figure is a modified version of [11] and [12].)

TABLE I
SATELLITE DATASETS CHARACTERISTICS

| Features | Imagery Type | | |
|---|---|---|---|
| | IKONOS | QUICKBIRD | LANDSAT 7 ETM+ |
| MS Image – Spectral Bands and Range | Blue (445-516 nm), Green (506-595 nm), Red (632-698 nm), NIR (757-853 nm) | Blue (450-520 nm), Green (520-600 nm), Red (630-690 nm), NIR (760-900 nm) | Blue (450-515 nm), Green (525-605 nm), Red (630-690 nm), NIR (760-900 nm), Mid IR (1550-1750 nm), Mid IR (2080-2350 nm), |
| Pan Image – Spectral Range | 450-900 nm | 450-900 nm | 520-920 nm |
| Spatial Resolution MS Image | 4 m | 2.4 m | 28.5 m |
| Spatial Resolution Pan Image | 1 m | 0.6 m | 14.25 m |
| Resolution Ratio of MS and Pan Image | 4 | 4 | 2 |
| Radiometric Resolution | 11 | 11 | 8 |

wavelet transform [12], [20]. The building block of the NSCT is 2-D two-channel nonsubsampled filter banks (NFSBs). To have perfect reconstruction, these far-infrared two-channel NSFBs are constructed to satisfy the Bezout identity

$$H_0(z)G_0(z) + H_1(z)G_1(z) = 1 \tag{5}$$

where $H(z)$ represents the $z$-transform of the 2-D filter. $H_0(z)$ and $H_1(z)$ represent the 2-D low-pass and high-pass analysis filters, whereas $G_0(z)$ and $G_1(z)$ are the low-pass and high-pass synthesis filters. For filter design, additional constraints for frequency response are also imposed to have a good solution [12].

The NSCT is also obtained via a two stage non shift-invariant process [12], [20]. The first part achieves the multiscale property, while the second part provides directionality information. Both stages of the NSCT are constructed to be invertible to have an overall invertible system. Fig. 3 shows an overview of the NSCT.

The nonsubsampled pyramid (NSP) subband decomposition for two levels $(J = 2)$ and the frequency subband division are shown in Fig. 4. This stage is conceptually similar to the separable 1-D nonsubsampled wavelet transform (NSWT) computed with the à trous method [28]. In contrast to NSWT, the NSP decomposition is obtained via nonsubsampled 2-D filter banks. After the first level of decomposition, the filters are upsampled for subsequent levels to obtain the multiscale property. Fig. 4(a) shows the subbands division obtained by the two-level NSP. This figure clearly shows that the low-pass filter supports the frequency region of $[-(\pi/2^j), -(\pi/2^j)]$ at the $j$th stage, whereas the high-pass filter supports the complement region $[-(\pi/2^{j-1}), -(\pi/2^{j-1})]$ to $[-(\pi/2^j), -(\pi/2^j)]$.

TABLE II
DATASETS' SUMMARY

| | Ik1 | Ik2 | Ik3 | Qb1 | Qb2 | Ld1 | Ld2 |
|---|---|---|---|---|---|---|---|
| Locations | Brookings, SD, USA | San Diego, CA, USA | Volga, SD, USA | Boulder, CO, USA | Boulder, CO, USA | Boulder, CO, USA | Starkville, MS, USA |
| MS Image Size | 512 x 512 | 500 x 500 | 512 x 512 | 512 x 512 | 512 x 512 | 512 x 512 | 1024 x 1024 |
| Pan Image Size | 2048 x 2048 | 2000 x 2000 | 2048 x 2048 | 2048 x 2048 | 2048 x 2048 | 1024 x 1024 | 2048 x 2048 |

At each stage of the NSWT process, three directional images are generated that result in an overall redundancy of $3J + 1$, whereas the NSP stage produces only a $J + 1$ redundancy [12].

The second stage of the nonsubsampled directional filter bank (NSDFB) structure of the NSCT provides directional information. The computational complexity is the same as the building block of NSFB. The NSDFB is obtained by a combination of the critically sampled two-channel fan filters and the resampling operation that helps to split the 2-D frequency plane in directional wedges [29]. The directional frequency decomposition (four in this case), constructed via cascading two two-channel fan filters, is shown in Fig. 5. The finer detailed direction for subsequent stages is obtained by discretely upsampling the filters by a quincunx matrix $Q$ to take into account aliasing effect for the directional response [12]. The redundancy of the $J$-level NSCT is given by $1 + \sum_{j=1}^{J} 2^{d_j}$ where $d_j$ is the number of levels in the NSDFB at the $j$th scale.

This study uses both the subsampled and nonsubsampled versions of the contourlet transform to examine its effectiveness for pan-sharpening.

### C. Improved Adaptive PCA–Contourlet Merger Pan-Sharpening Method

The first step of the pan-sharpening process is coregistering the MS image and the PAN image and resizing the MS image to the size of the PAN image. This step is performed regardless of the method used for pan-sharpening. The steps for the PCA–contourlet method are described as follows.

- Perform an adaptive-PCA transformation along the spectral axis for PC selection, as described in Section III-A.
- Histogram match the PAN image to the PC image selected for injection of high detailed information.
- Apply the CT spatial transformation along the spatial dimension of the selected PC and PAN images.
- Replace only the detail contourlet coefficients of the selected PC image by the detail contourlet coefficients obtained by transformation of the histogram matched PAN image.
- Perform inverse spatial and spectral transformations to obtain the pan-sharpened image.

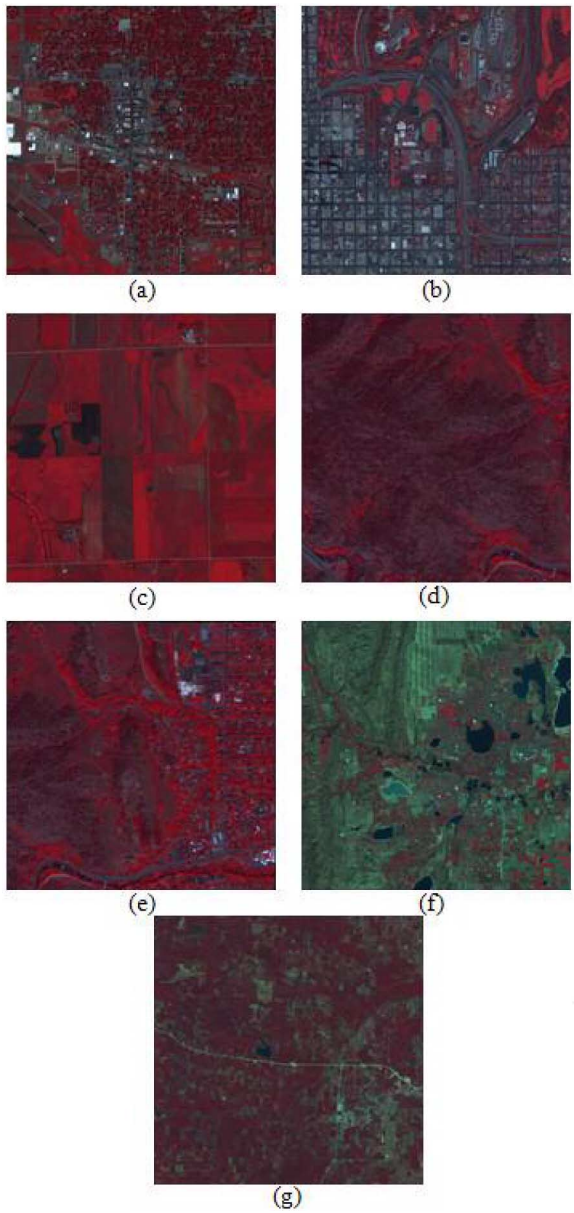


Fig. 6. False color imagery of the datasets. (a) IKONOS scene—Ik1. (b) IKONOS scene—Ik2. (c) IKONOS scene—Ik. (d) QuickBird scene—Qb1. (e) QuickBird scene—Qb2. (f) Landsat-7 ETM+—Ld1. (g) Landsat-7 ETM+—Ld2.

## IV. DATASETS AND EXPERIMENTAL RESULTS

### A. Experimental Datasets

The presented method is evaluated by performing pan sharpening on datasets acquired by IKONOS, QuickBird, and Landsat-7 ETM+ satellites. All images are radiometrically calibrated and orthorectified to uniform ground resolution. The MS and PAN images are coregistered for each dataset. All imageries have different characteristics in terms of spectral bands and range, spatial and radiometric resolutions, etc. These characteristics are summarized in Table I. Table II represents a summary of the datasets as related to their size and location.

TABLE III
DATASETS' STATISTICS

| Image Set | PC | Zero mean MS bands | | Standardardize(Std) MS band by zero mean and unit variance | |
|---|---|---|---|---|---|
| | | Variances (%) | CC with Pan | Variances (%) | CC with Pan |
| ik1 | First | 80.666 | 0.813 | 79.401 | **0.818** |
| | Second | 18.558 | 0.238 | 19.685 | 0.221 |
| | Third | 0.681 | 0.001 | 0.829 | -0.015 |
| | Fourth | 0.094 | -0.021 | 0.084 | -0.020 |
| ik2 | First | 69.754 | **-0.714** | 75.211 | -0.687 |
| | Second | 29.718 | -0.382 | 24.152 | -0.429 |
| | Third | 0.492 | 0.008 | 0.597 | 0.016 |
| | Fourth | 0.036 | -0.001 | 0.040 | 0.000 |
| ik3 | First | 85.610 | -0.797 | 76.309 | -0.091 |
| | Second | 13.898 | -0.441 | 21.096 | **-0.904** |
| | Third | 0.416 | 0.010 | 2.097 | 0.069 |
| | Fourth | 0.076 | 0.037 | 0.498 | 0.009 |
| qb1 | First | 60.393 | **0.666** | 74.245 | 0.541 |
| | Second | 39.152 | -0.310 | 24.840 | 0.496 |
| | Third | 0.397 | -0.036 | 0.751 | -0.055 |
| | Fourth | 0.057 | -0.006 | 0.164 | 0.000 |
| qb2 | First | 53.383 | 0.324 | 73.768 | 0.512 |
| | Second | 45.952 | **-0.677** | 25.097 | -0.547 |
| | Third | 0.611 | -0.048 | 1.047 | -0.070 |
| | Fourth | 0.055 | -0.005 | 0.088 | -0.003 |
| ld1 | First | 74.754 | 0.800 | 71.635 | **0.836** |
| | Second | 24.127 | 0.496 | 27.039 | 0.434 |
| | Third | 1.119 | -0.029 | 1.326 | 0.002 |
| ld2 | First | 87.271 | -0.717 | 67.185 | **-0.779** |
| | Second | 12.227 | 0.537 | 32.315 | 0.442 |
| | Third | 0.502 | -0.021 | 0.500 | -0.001 |

The false color sample imageries used for the experiments are shown in Fig. 6.

*1) IKONOS Datasets:* Three IKONOS datasets Ik1–Ik3 used in this study are shown in Fig. 6(a)–(c). Ik1 is a scene consisting of urban features such as airport runway, buildings, and natural features such as forests. Ik2 is a scene from an urban area that consists of man-made buildings and curved roads. Ik3 mostly has agricultural lands; urban features in this image are minimal.

*2) Quickbird Datasets:* Two QuickBird imageries, Qb1 and Qb2, are shown in Fig. 6(d), (e). Qb1 is an imagery representing mountainous regions consisting of forest and having a lot of uniform texture details, while the dataset Qb2 has natural features such as forest regions and urban features such as man-made buildings.

*3) Landsat-7 ETM+ Datasets:* Two Landsat-7 ETM+ imageries, Ld1 and Ld2, are shown in Fig. 6(f), (g). Because only three bands are within the wavelength span of the PAN image, only the green, red, and near-infrared bands are considered for pan-sharpening. Ld1 is a scene representing mountainous regions consisting of natural features such as lakes and forest, and urban features such as buildings, and Ld2 has more agricultural content.

### B. Experimental Results

Experiments are conducted to show the effectiveness of the presented adaptive PCA–contourlet merger method using Wald's protocol [30]. Hence, the MS and PAN images are degraded by the resolution ratio. Pan-sharpening is performed on the images at the degraded scale. The global quality indexes are calculated by comparing the pan-sharpened image with the original MS image. These commonly known global quality indexes are the Spectral Angle Mapper (SAM) [31], Spectral Information Divergence (SID) [32], relative dimensionless global error in synthesis (ERGAS) [33], Relative Average Spectral Error (RASE) [34], and universal image quality index $(Q)$ [35]. Note that the SAM and SID criteria values correspond to average values computed based on the spectral fidelity of the pixels in an image.

*1) Experiment 1—Adaptive PCA and Traditional PCA Comparison:* Because PCA is data dependent, the statistics of the PCs are obtained from the sample imagery using two different approaches—standardizing each MS band by making it zero mean and unit variance and subtracting only the mean from the MS band. The difference between the two approaches is that in the first approach, all the MS bands have a uniform variance of one, whereas in the second approach the variance is not uniform for all bands. Accordingly, this does affect the cross correlation between the PCs and PAN images as shown in Table III, which illustrates the statistics, variance, and cross correlation, obtained from both approaches for all the sample imagery. These are approaches of normalizing the data before applying the PCA method. When each MS band has a uniform variance, using variance values other than unity does not affect the cross-correlation value between the PC and PAN images. This table also indicates that a higher variance of the PC components does not always guarantee a higher correlation of the components

TABLE IV
TRADITIONAL PCA VERSUS ADAPTIVE PCA COMPARISON

| Image | Method | ERGAS | RASE (%) | SAM | SID | Qavg | PC-Replaced | Normalization | Sign Adjust Pan Image |
|---|---|---|---|---|---|---|---|---|---|
| Ik-1 | Envi - PCA | 2.442 | 21.143 | 7.995 | 9690.3 | 0.875 | 1 | 0 | No |
| | STD - PCA | 2.441 | 21.135 | 7.998 | 9709.4 | 0.875 | 1 | 0 | No |
| | ADAPT-PCA | **2.411** | **20.790** | **7.872** | **9546.6** | **0.879** | 1 | 1 | No |
| Ik-2 | Envi - PCA | **1.995** | **16.109** | **5.275** | **3581.6** | **0.849** | 1 | 0 | No |
| | STD - PCA | 5.784 | 47.592 | 8.238 | 11779.8 | -0.381 | 1 | 0 | No |
| | ADAPT-PCA | **1.995** | **16.109** | **5.275** | **3581.5** | **0.849** | 1 | 0 | Yes |
| Ik-3 | Envi - PCA | 5.665 | 45.693 | 12.134 | 27618.5 | 0.270 | 1 | 0 | No |
| | STD - PCA | 5.665 | 45.693 | 12.134 | 27611.4 | 0.270 | 1 | 0 | No |
| | ADAPT-PCA | **0.888** | **8.570** | **2.051** | **1263.3** | **0.899** | 2 | 1 | Yes |
| qb-1 | Envi - PCA | 1.567 | 12.903 | 4.015 | 2261.3 | 0.866 | 1 | 0 | No |
| | STD - PCA | 1.567 | 12.903 | 4.015 | 2261.0 | 0.866 | 1 | 0 | No |
| | ADAPT-PCA | 1.567 | 12.903 | 4.015 | 2261.0 | 0.866 | 1 | 0 | No |
| qb-2 | Envi - PCA | 3.030 | 30.069 | 11.152 | 21376.3 | 0.584 | 1 | 0 | No |
| | STD - PCA | 3.030 | 30.069 | 11.152 | 21367.3 | 0.584 | 1 | 0 | No |
| | ADAPT-PCA | **1.980** | **17.373** | **4.679** | **3657.4** | **0.880** | 2 | 0 | Yes |
| ld-1 | Envi - PCA | 4.511 | 15.063 | 3.233 | 1978.0 | 0.840 | 1 | 0 | No |
| | STD - PCA | 4.508 | 15.052 | 3.223 | 1971.8 | 0.840 | 1 | 0 | No |
| | ADAPT-PCA | **4.131** | **13.851** | **2.981** | **1718.7** | **0.861** | 1 | 1 | No |
| ld-2 | Envi - PCA | 3.965 | 16.400 | 5.542 | 22035.9 | 0.794 | 1 | 0 | No |
| | STD - PCA | 9.360 | 39.591 | 10.627 | 76281.4 | -0.186 | 1 | 0 | No |
| | ADAPT-PCA | **3.564** | **14.666** | **4.757** | **16827.0** | **0.827** | 1 | 1 | Yes |

Note: *Normalization* 1 indicates that the MS band is normalized to have a zero mean and unit variance, while *normalization* 0 indicates that the MS band is normalized to have only a zero mean.

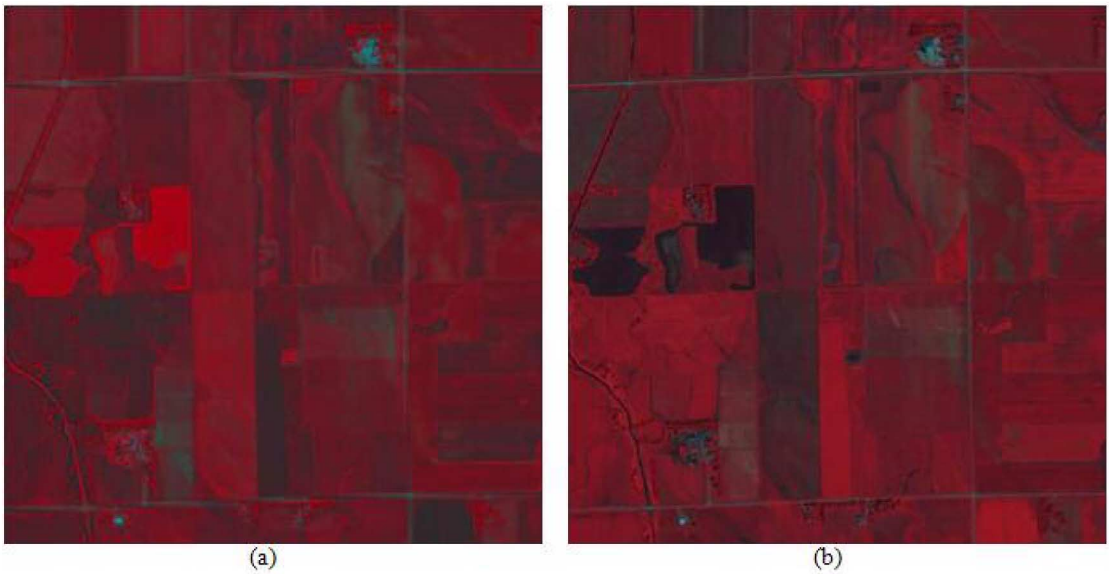


Fig. 7. PCA–pan-sharpening results for dataset Ik3. (a) ENVI–PCA. (b) Adaptive PCA.

with the PAN image. Additionally, a strong negative correlation value between the PC components and the PAN image provides information regarding the sign adjustments.

The first aim of this paper is to show the advantage of using the adaptive PCA approach over the standard PCA approach that has been used since the last decade for pan-sharpening. Hence, comparison is only performed between the standard PCA approach available in the commercial software ENVI, similar implementation in Matlab, and the adaptive PCA approach. These are denoted by ENVI–PCA, STD–PCA, and ADAPT–PCA, respectively. Table IV shows the evaluation results of the pan-sharpened images using different methods in terms of well-known global indexes. These results clearly show the advantage of using the adaptive PCA approach when compared to the standard approach. This table also provides information on the selection process of the PC for replacement, normalization method used, and sign adjustment performed on the PAN image. For example, consider the results for the Ik3 dataset, which represents the agricultural field. If the standard PCA approach is used for pan-sharpening, the resulting image

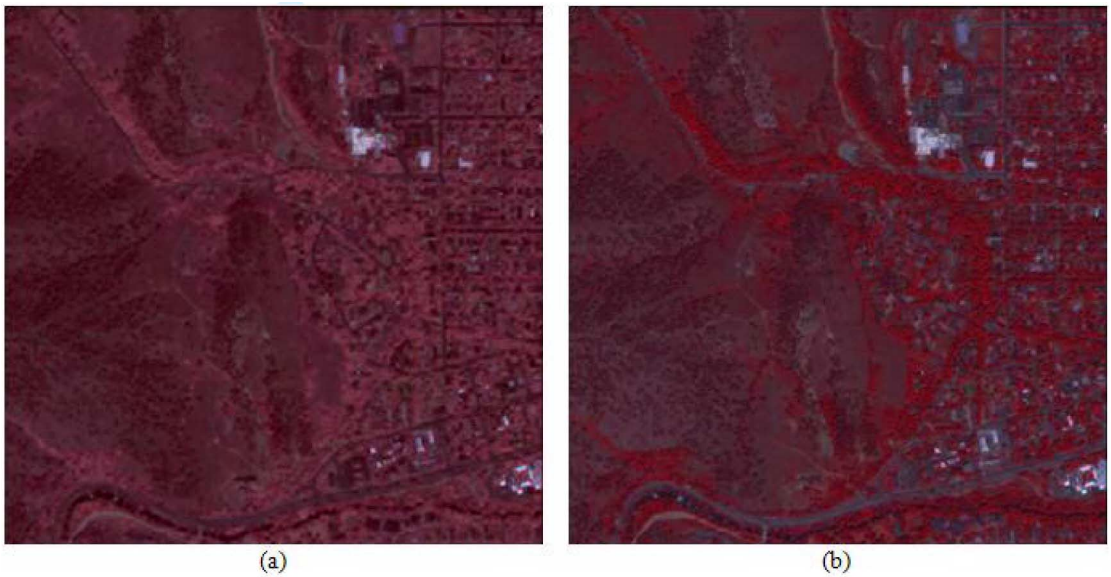


Fig. 8. PCA–pan-sharpening results for dataset Qb2. (a) ENVI–PCA. (b) Adaptive PCA.

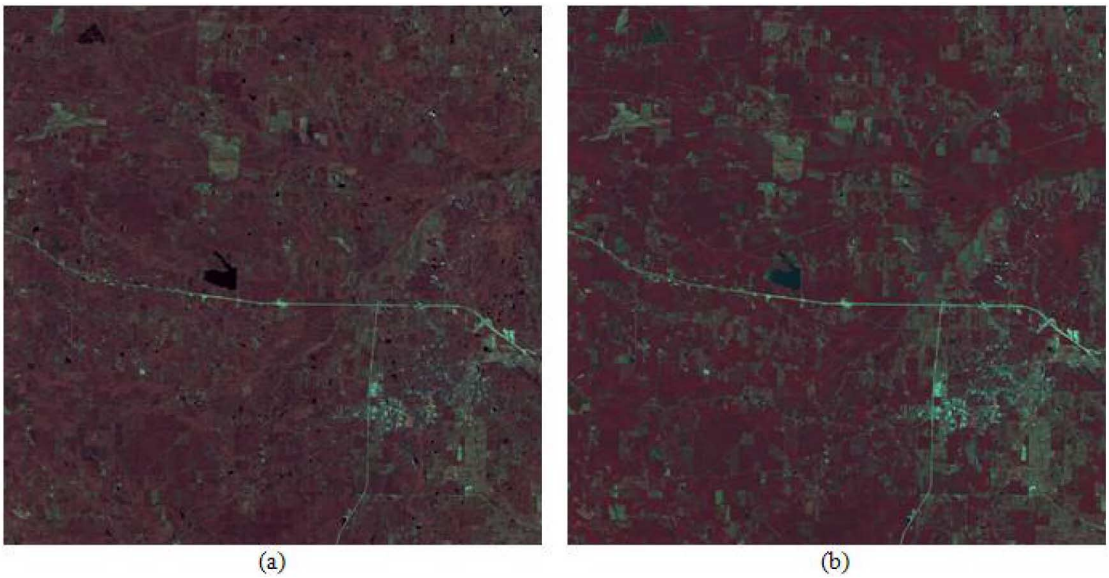


Fig. 9. PCA–pan-sharpening results for dataset Ld2. (a) ENVI–PCA. (b) Adaptive PCA.

has very high distortion, as indicated by an ERGAS value of 5.66. Generally, good pan-sharpening results will have an ERGAS value close to 0. With the use of the adaptive PCA approach, the ERGAS value for this dataset is reduced to 0.88, which shows a significant increase in the quality of the resulting image. Figs. 7–9 illustrate the corresponding pan-sharpened images using the ENVI–PCA and the ADAPT–PCA for datasets Ik3, Qb1, and Ld2. A visual inspection also reveals that the adaptive PCA approach is better than the standard PCA approach.

*2) Experiment 2—Advantage of Contourlets Over Wavelets:* The second aim of this paper is to show that contourlet transformation is a better transformation approach than the wavelet for pan-sharpening. The comparison performed here is only between the combined PCA–wavelet method [2] and the PCA–contourlet method. The subsampled PCA–contourlet transformation and the nonsubampled versions are denoted by PCA–CT and PCA–NSCT, respectively, and PCA–WT and PCA–RDWT denote the PCA–wavelet-based method for subsampled and nonsubsampled versions, respectively.

A decomposition level selection for a dataset is based on its resolution ratio [36]. For the IKONOS and QuickBird imagery, a two-scale decomposition level is performed, whereas for the Landsat-7 ETM+ image, a one-scale decomposition level is used for this experiment. For the wavelet transform, the db10 mother wavelet is used, whereas for the contourlet transform, the available pyramid 2-D–filter maxflat and dmaxflat are used for the directional filter banks.

Table V compares results between the subsampled PCA-wavelet and the PCA-contourlet approaches. For all the sample imagery in this study this table indicates that the pan-sharpened image obtained using the PCA–contourlet approach has better quality. To statistically evaluate the difference between the two methods, the paired t-test and the Wilcoxon matched-pairs

TABLE V
SUBSAMPLED PCA–CONTOURLET VERSUS PCA–WAVELET COMPARISON

| Image | Method | ERGAS | RASE (%) | SAM | SID | Qavg |
|---|---|---|---|---|---|---|
| Ideal | | 0 | 0 | 0 | 0 | 1 |
| ik-1 | PCA-CT | **2.314** | **19.007** | 7.157 | 9188.9 | **0.905** |
| | PCA-WT | 2.384 | 19.749 | **7.115** | **8932.5** | 0.898 |
| ik-2 | PCA-CT | **3.333** | **27.156** | **4.162** | **2367.9** | **0.614** |
| | PCA-WT | 3.394 | 27.673 | 4.335 | 2513.9 | 0.596 |
| ik-3 | PCA-CT | **1.981** | **16.358** | **3.317** | **2896.0** | **0.864** |
| | PCA-WT | 2.009 | 16.600 | 3.438 | 3074.8 | 0.859 |
| qb-1 | PCA-CT | **1.263** | **11.054** | **3.797** | 2139.7 | **0.887** |
| | PCA-WT | 1.316 | 11.432 | 3.799 | **2125.0** | 0.881 |
| qb-2 | PCA-CT | 2.508 | **21.189** | **6.620** | **9243.0** | **0.845** |
| | PCA-WT | **2.507** | 21.662 | 6.752 | 9510.9 | 0.830 |
| ld-1 | PCA-CT | **2.748** | **9.352** | **2.448** | 1138.4 | **0.940** |
| | PCA-WT | 2.836 | 9.645 | 2.453 | **1135.4** | 0.936 |
| ld-2 | PCA-CT | **3.670** | **14.929** | **3.309** | **7055.3** | **0.824** |
| | PCA-WT | 3.704 | 15.082 | 3.349 | 7230.3 | 0.821 |

TABLE VI
STATISTICAL TEST OF SUBSAMPLED PCA–CONTOURLET VERSUS PCA-WAVELET METHODS

| Test | | ERGAS | RASE (%) | SAM | SID | Qavg |
|---|---|---|---|---|---|---|
| Paired T-Test | h at (5%) | 1 | 1 | 0 | 0 | 1 |
| | p-Value | 0.0054 | 0.0017 | 0.0893 | 0.3311 | 0.0093 |
| Wilcoxon Matched Pairs Signed Ranks Test | h at (5%) | 1 | 1 | 0 | 0 | 1 |
| | p-Value | 0.0313 | 0.0156 | 0.1094 | 0.4688 | 0.0156 |

TABLE VII
NONSUBSAMPLED PCA–CONTOURLET VERSUS PCA–WAVELET COMPARISON

| Image | Method | ERGAS | RASE (%) | SAM | SID | Qavg |
|---|---|---|---|---|---|---|
| Ideal | | 0 | 0 | 0 | 0 | 1 |
| ik-1 | PCA-NSCT | **2.271** | **18.745** | 7.410 | 9875.9 | **0.909** |
| | PCA-RDWT | 2.272 | 18.745 | **7.405** | **9794.5** | 0.908 |
| ik-2 | PCA-NSCT | **3.322** | **27.063** | **4.197** | **2355.0** | **0.605** |
| | PCA-RDWT | 3.343 | 27.245 | 4.224 | 2369.3 | 0.590 |
| ik-3 | PCA-NSCT | **1.952** | **16.153** | **3.268** | **2817.3** | **0.863** |
| | PCA-RDWT | 1.960 | 16.217 | 3.306 | 2849.5 | 0.862 |
| qb-1 | PCA-NSCT | **1.267** | **11.122** | **3.764** | **2096.9** | **0.884** |
| | PCA-RDWT | 1.280 | 11.214 | 3.767 | 2099.7 | 0.883 |
| qb-2 | PCA-NSCT | **2.485** | **21.221** | 6.631 | 9181.8 | **0.839** |
| | PCA-RDWT | 2.491 | 21.260 | **6.616** | **9134.6** | **0.839** |
| ld-1 | PCA-NSCT | **2.708** | **9.220** | **2.434** | **1125.0** | **0.941** |
| | PCA-RDWT | 2.711 | 9.229 | 2.436 | 1128.0 | 0.941 |
| ld-2 | PCA-NSCT | **3.636** | **14.773** | 3.189 | **6515.0** | **0.824** |
| | PCA-RDWT | 3.665 | 14.901 | **3.183** | 6521.8 | 0.820 |

TABLE VIII
STATISTICAL TEST OF SUBSAMPLED PCA–CONTOURLET VERSUS PCA–WAVELET METHODS

| Test | | ERGAS | RASE | SAM | SID | Qavg |
|---|---|---|---|---|---|---|
| Paired T-Test | h at (5%) | 1 | 1 | 0 | 0 | 0 |
| | p-Value | 0.0239 | 0.0254 | 0.4180 | 0.5330 | 0.1744 |
| Wilcoxon Matched Pairs Signed Ranks Test | h at (5%) | 1 | 1 | 0 | 0 | 0 |
| | p-Value | 0.0156 | 0.0313 | 0.8125 | 0.9375 | 0.0625 |

test have been performed on different evaluation indexes (see Table VI). Based on the ERGAS, RASE, and the $Q_{\text{avg}}$ values, the null hypothesis, indicating a similarity (equality) between the two methods is rejected with a confidence level of 95%, whereas we fail to reject the null hypothesis based on the average SAM and SID values. Similarly, Table VII provides a comparison between the nonsubsampled PCA wavelets and the PCA contourlets. The results presented in this table again show that, in general, contourlets are better than wavelets for spatial transformation. The statistical evaluation results for this

TABLE IX
ADAPTIVE PCA–CONTOURLET MERGER VERSUS TRADITIONAL PCA–CONTOURLET MERGER COMPARISON

| Image | Method | ERGAS | RASE (%) | SAM | SID | Qavg |
|---|---|---|---|---|---|---|
| Ideal | | 0 | 0 | 0 | 0 | 1 |
| ik-1 | PCA-NSCT | 2.271 | 18.745 | 7.410 | 9875.9 | 0.909 |
| | APCA-NSCT | **2.257** | **18.622** | **7.350** | **9716.4** | **0.910** |
| ik-2 | PCA-NSCT | 3.322 | 27.063 | **4.197** | **2355.0** | 0.605 |
| | APCA-NSCT | **1.616** | **12.817** | 4.448 | 2794.6 | **0.918** |
| ik-3 | PCA-NSCT | 1.952 | 16.153 | 3.268 | 2817.3 | 0.863 |
| | APCA-NSCT | **0.854** | **8.378** | **1.955** | **1078.0** | **0.900** |
| qb-1 | PCA-NSCT | 1.267 | 11.122 | 3.764 | 2096.9 | 0.884 |
| | APCA-NSCT | 1.267 | 11.122 | 3.764 | 2096.9 | 0.884 |
| qb-2 | PCA-NSCT | 2.485 | 21.221 | 6.631 | 9181.8 | 0.839 |
| | APCA-NSCT | **1.653** | **15.468** | **4.379** | **3425.3** | **0.896** |
| ld-1 | PCA-NSCT | 2.708 | 9.220 | 2.434 | 1125.0 | 0.941 |
| | APCA-NSCT | **2.697** | **9.183** | **2.403** | **1094.6** | **0.942** |
| ld-2 | PCA-NSCT | 3.636 | 14.773 | 3.189 | 6515.0 | 0.824 |
| | APCA-NSCT | **2.509** | **9.834** | **3.140** | **6223.2** | **0.911** |

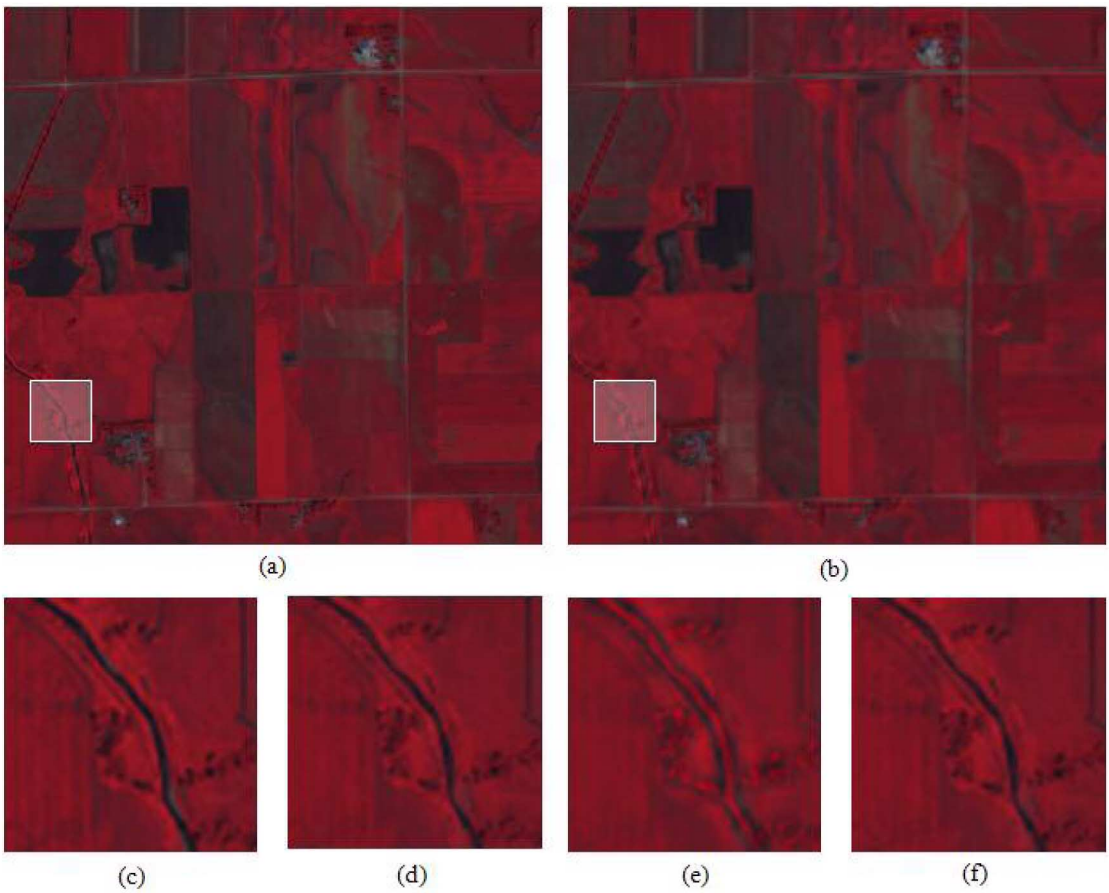


Fig. 10. Combined PCA–contourlet pan-sharpening results for dataset Ik3. (a) APCA–NSCT. (b) PCA–NSCT. (c) Original subset image. (d) Subset image APCA–NSCT. (e) Subset image PCA–NSCT. (f) Subset image APCA–RDWT.

case are tabulated in Table VIII. Based on the ERGAS and RASE values, the null hypothesis that both algorithms are equal is rejected with a confidence level of 95%, whereas based on the average $Q$, SAM, and SID values, we fail to reject the null hypothesis. Similar to wavelets, these tables also illustrate that the nonsubsampled contourlet transformation is a better approach for pan-sharpening then the subsampled approach.

*3) Experiment 3—Combined Adaptive PCA Approach and Contourlets:* Finally, this experiment aims to show the advantage of combining the adaptive PCA approach with the nonsubsampled contourlet transform (APCA–NSCT). Table IX shows the results obtained by the APCA–NSCT method and makes a performance comparison with the standard PCA–contourlet approach. These results again show that for the datasets in

TABLE X
ADAPTIVE PCA–CONTOURLET MERGER VERSUS ADAPTIVE PCA–WAVELET MERGER COMPARISON

| Image | Method | ERGAS | RASE (%) | SAM | SID | Qavg |
|---|---|---|---|---|---|---|
| Ideal | | 0 | 0 | 0 | 0 | 1 |
| ik-1 | APCA-NSCT | **2.257** | **18.622** | **7.350** | **9716.4** | **0.910** |
| | APCA-RDWT | 2.261 | 18.674 | 7.358 | 9750.3 | 0.909 |
| ik-2 | APCA-NSCT | **1.616** | **12.817** | **4.448** | **2794.6** | **0.918** |
| | APCA-RDWT | 1.633 | 12.965 | 4.461 | 2804.9 | 0.916 |
| ik-3 | APCA-NSCT | **0.854** | **8.378** | **1.955** | **1078.0** | **0.900** |
| | APCA-RDWT | 0.866 | 8.452 | 1.970 | 1087.1 | 0.899 |
| qb-1 | APCA-NSCT | **1.267** | **11.122** | **3.764** | **2096.9** | **0.884** |
| | APCA-RDWT | 1.280 | 11.214 | 3.767 | 2099.7 | 0.883 |
| qb-2 | APCA-NSCT | **1.653** | **15.468** | **4.379** | **3425.3** | 0.896 |
| | APCA-RDWT | 1.664 | 15.538 | 4.380 | 3433.3 | 0.896 |
| ld-1 | APCA-NSCT | **2.697** | **9.183** | **2.403** | 1094.6 | **0.942** |
| | APCA-RDWT | 2.717 | 9.257 | 2.404 | **1092.6** | 0.941 |
| ld-2 | APCA-NSCT | **2.509** | **9.834** | **3.140** | 6223.2 | **0.911** |
| | APCA-RDWT | 2.531 | 9.927 | 3.145 | **6206.3** | 0.910 |

TABLE XI
STATISTICAL TEST OF NONSUBSAMPLED ADAPTIVE PCA–CONTOURLET VERSUS ADAPTIVE PCA–WAVELET MERGER METHODS

| Test | | ERGAS | RASE (%) | SAM | SID | Qavg |
|---|---|---|---|---|---|---|
| Paired T-Test | h at (5%) | 1 | 1 | 1 | 0 | 1 |
| | p-Value | 0.0009 | 0.0003 | 0.0218 | 0.3074 | 0.0167 |
| Wilcoxon Matched Pairs Signed Ranks Test | h at (5%) | 1 | 1 | 1 | 0 | 0 |
| | p-Value | 0.0156 | 0.0156 | 0.0156 | 0.2969 | 0.0625 |

which the PAN image has low correlation with the first PC component, the APCA–NSCT method significantly outperforms the PCA–NSCT approach. Fig. 10 shows the resultant false color pan-sharpened image for the Ik3 dataset using the APCA-NSCT and the PCA-NSCT methods. A subset image of a region of interest is shown in Fig. 10(c)–(e), which clearly indicates spectral distortion resulting from the use of the PCA–NSCT method in the nonagricultural content area. However, spectral distortion is minimal on the thin water stream. Fig. 10(e) and (f) shows the comparison of the subset image using APCA–RDWT and APCA–NSCT. Careful observations of these figures show that for the APCA–RDWT approach, the water stream has a more reddish shade when compared to the APCA–NSCT. Visually it can be verified that the APCA–NSCT approach is better in preserving the spectral information of the multispectral image. Table X compares the nonsubsampled APCA–RDWT and the APCA–NSCT. The results presented in this table again show that the merger of the adaptive PCA with NSCT works better than the APCA–RDWT merger. Table XI provides a statistical test for both methods. This table shows that, based on the ERGAS, RASE, SAM, and $Q$ values, there is sufficient evidence at the 95% significance level to reject the claim that both methods are equal. Thus, statistically, it seems that the merger of APCA and NSCT produces better results when compared to the merger of APCA and RDWT.

## V. CONCLUSION

This paper presents a new method of pan-sharpening based on the merger of the adaptive PCA and the contourlet transform. The adaptive PCA approach helps in preserving the spectral information, whereas the contourlet, which is known to have better directional representation than the wavelet, provides efficient spatial transformation for injection of high detail information. In general, the merger of the adaptive PCA–contourlet method provides better fusion results based on well-known global indexes. Also, pan-sharpening obtained from the use of the nonsubsampled contourlet transform provides better results than the subsampled approach. Filter selection plays an important role when using the contourlet or wavelet transform approaches. Further research is necessary in this regard.

## ACKNOWLEDGMENT

The IKONOS, QuickBird, and Landsat-7 ETM+ imagery were obtained from Space Imaging, DigitalGlobe, and Global Land Cover Facility (GLCF), University of Maryland, respectively.

## REFERENCES

[1] G. A. Shaw and H. K. Burke, "Spectral imaging for remote sensing," *Lincoln Lab. J.*, vol. 14, no. 1, pp. 3–28, 2003.
[2] M. Gonzalez-Audicana, J. L. Saleta, R. G. Catalan, and R. Garcia, "Fusion of multispectral and panchromatic images using improved IHS and PCA mergers based on wavelet decomposition," *IEEE Trans. Geosci. Remote Sens.*, vol. 42, no. 6, pp. 1291–1299, Jun. 2004.
[3] Y. Zhang, "Understanding image fusion," *Photogramm. Eng. Remote Sens.*, vol. 70, no. 6, pp. 657–661, Jun. 2004.
[4] A. Garzelli, F. Nencini, L. Alparone, B. Aiazzi, and S. Baronti, "Pan sharpening of multispectral image: A critical review and comparison," in *Proc. IGARSS*, Anchorage, AK, 2004, vol. 1, pp. 81–84.
[5] V. K. Shettigara, "A generalized component substitution technique for spatial enhancement of multispectral images using a higher resolution

data set," *Photogramm. Eng. Remote Sens.*, vol. 58, no. 5, pp. 561–567, 1992.
[6] C. Pohl and J. L. Van Genderen, "Multisensor image fusion in remote sensing: Concepts, methods, and applications," *Int. J. Remote Sens.*, vol. 19, no. 5, pp. 823–854, Mar. 1998.
[7] J. Zhou, D. L. Civco, and J. A. Silander, "A wavelet transform method to merge LandSat TM and SPOT panchromatic data," *Int. J. Remote Sens.*, vol. 19, no. 4, pp. 743–757, Mar. 1998.
[8] Y. Zhang, "A new merging method and its spectral and spatial effects," *Int. J. Remote Sens.*, vol. 20, no. 10, pp. 2004–2014, Jul. 1999.
[9] B. Aiazzi, L. Alparone, S. Baronti, and A. Garzelli, "Context-driven fusion of high spatial and spectral resolution images based on oversampled multiresolution analysis," *IEEE Trans. Remote Sens.*, vol. 40, no. 10, pp. 2300–2312, Oct. 2002.
[10] J. Nunez, X. Otazu, O. Fors, A. Prades, V. Pala, and R. Arbiol, "Multiresolution-based image fusion with additive wavelet decomposition," *IEEE Trans. Geosci. Remote Sens.*, vol. 37, no. 3, pp. 1204–1211, May 1999.
[11] M. N. Do and M. Vetterli, "The contourlet transform: An efficient directional multiresolution image representation," *IEEE Trans. Image Process.*, vol. 14, no. 12, pp. 2096–2106, Dec. 2005.
[12] A. L. Cunha, J. Zhou, and M. N. Do, "The nonsubsampled contourlet transform: Theory, design, and applications," *IEEE Trans. Image Process.*, vol. 15, no. 10, pp. 3089–3101, Oct. 2006.
[13] Q. Miao and B. Wang, "The contourlet transform for image fusion," *Proc. SPIE*, vol. 4, p. 624 20Z.1, 2006.
[14] Y. Zheng, C. Zhu, J. Song, and X. Zhao, "Fusion of multi-band SAR images based on contourlet transform," in *Proc. IEEE Int. Conf. Inf. Acquisition*, 2006, pp. 420–424.
[15] P. S. Chavez and A. Y. Kwarteng, "Extracting spectral contrast in Landsat Thematic Mapper image data using selective principal component analysis," *Photogramm. Eng. Remote Sens.*, vol. 55, no. 3, pp. 339–348, Mar. 1989.
[16] R. Duda and P. Hart, *Pattern Classification and Scene Analysis*. New York: Wiley, 1996. Preliminary Edition.
[17] V. K. Shettigara, "A generalized component substitution technique for spatial enhancement of multispectral images using a higher resolution data set," *Photogramm. Eng. Remote Sens.*, vol. 58, no. 5, pp. 561–567, 1992.
[18] V. Meenakshisundaram, "Quality assessment of IKONOS and QuickBird fused images for urban mapping," M.S. thesis, Univ. Calgary, Calgary, AB, Canada, 2005.
[19] M. N. Do and M. Vetterli, "Framing pyramids," *IEEE Trans. Signal Process.*, vol. 51, no. 9, pp. 2329–2342, Sep. 2003.
[20] J. Zhou, A. L. Cunha, and M. N. Do, "Nonsubsampled contourlet transform: Construction and application in enhancement," in *Proc. IEEE Int. Conf. Image*, Sep. 2005, vol. 1, pp. 469–472.
[21] A. L. Cunha and M. N. Do, "Filter design for directional multiresolution decomposition," in *Proc. SPIE—Wavelet XI*, Sep. 17, 2005, vol. 5914, pp. 256–265.
[22] J. Daugman, "Two-dimensional spectral analysis of cortical receptive field profiles," *Vis. Res.*, vol. 20, no. 10, pp. 847–856, 1980.
[23] A. B. Watson, "The cortex transform: Rapid computation of simulated neutral images," *Comput. Vis., Graph. Image Process.*, vol. 39, no. 3, pp. 311–327, 1987.
[24] E. P. Simoncelli, W. T. Freeman, E. H. Adelson, and D. J. Heeger, "Shiftable multiscale transforms," *IEEE Trans. Inf. Theory*, vol. 38, no. 2, pp. 587–607, Mar. 1992.
[25] J. P. Antoine, P. Carrette, R. Murenzi, and B. Piette, "Image analysis with two dimensional continuous wavelet transform," *Signal Process.*, vol. 31, no. 3, pp. 241–272, Apr. 1993.
[26] F. G. Meyerand and R. R. Coifman, "Brushlets: A tool for directional image analysis and image compression," *Appl. Comput. Harmon. Anal.*, vol. 4, no. 2, pp. 147–187, Apr. 1997.
[27] M. Vetterli, "Multidimensional subband coding: Some theory and algorithms," *Signal Process.*, vol. 6, no. 2, pp. 97–112, Feb. 1984.
[28] M. J. Shensa, "The discrete wavelet transform: Wedding the a-trous and Mallat algorithm," *IEEE Trans. Signal Process.*, vol. 40, no. 10, pp. 2464–2482, Oct. 1992.
[29] R. H. Bamberger and M. J. T. Smith, "A filter bank for the directional decomposition of images: Theory and design," *IEEE Trans. Signal Process.*, vol. 40, no. 4, pp. 882–893, Apr. 1992.
[30] L. Wald, T. Ranchin, and M. Mangolini, "Fusion of satellite images of different spatial resolutions: Assessing the quality of resulting images," *Photogramm. Eng. Remote Sens.*, vol. 63, no. 6, pp. 691–699, 1997.
[31] R. H. Yuhas, A. F. H. Goetz, and J. W. Boardman, "Discrimination among semi-arid landscape endmembers using the spectral angle mapper (SAM) algorithm," in *Proc. Summaries 3rd Annu. JPL Airborne Geosci. Workshop*, 1992, pp. 147–149.
[32] C. Chang, "Spectral Information divergence for hyperspectral image analysis," in *Proc. Geosci. Remote Sens. Symp.*, 1999, vol. 1, pp. 509–511.
[33] L. Wald, "Quality of high resolution synthesized images: Is there a simple criterion?" in *Proc. Int. Conf. Fusion Earth Data*, Jan. 2000, pp. 99–105.
[34] T. Ranchin and L. Wald, "Fusion of high spatial and spectral resolution images: The ARSIS concept and its implementation," *Photogramm. Eng. Remote Sens.*, vol. 66, no. 1, pp. 49–61, 2000.
[35] Z. Wang and A. C. Bovik, "A universal image quality index," *Signal Process. Lett.*, vol. 9, no. 3, pp. 81–84, Mar. 2002.
[36] P. S. Pradhan, R. L. King, N. H. Younan, and D. W. Holcomb, "Estimation of the number of decomposition levels for a wavelet based multiresolution multi-sensor image fusion," *IEEE Trans. Geosci. Remote Sens.*, vol. 44, no. 12, pp. 3674–3686, Dec. 2006.

**Vijay P. Shah** (S'00–M'07) received the B.E. degree in electrical engineering from Gujarat University, Gujarat, India, in 2000, the M.S. degree in electrical engineering from Mississippi State University, Mississippi State, in 2002, and the Ph.D. degree in computer engineering from Mississippi State University in 2007.

He is currently a Postdoctoral Fellow with SAIC-Frederick, Inc. at the National Cancer Institute (National Institutes of Health), Bethesda, MD. He had worked at the GeoResources Institute, Mississippi State University, as a Graduate Research Assistant from May 2004 to August 2007. His current research interests includes application of image information mining, data fusion, image segmentation, image compression, image reconstruction techniques to remote sensing imagery and biomedical imagery.

Dr. Shah received a Barrier Fellowship (fall 2001, spring 2002, spring 2004, and summer 2004) at Mississippi State University.

**Nicolas H. Younan** (S'87–M'88–SM'99) received the B.S.E.E. and M.S.E.E. degrees from Mississippi State University, Mississippi State, in 1982 and 1984, respectively, and the Ph.D. degree from Ohio University, Athens, in 1988.

He joined the faculty in the Department of Electrical, Computer Engineering, Mississippi State University as a Visiting Assistant Professor in 1988 and is currently a Professor and the Graduate Program Director in the department. His current research activities include signal and image analysis with applications to remote sensing, image information mining, automated target recognition, data fusion, and estimation/detection.

Dr. Younan is a member of Sigma Xi, Tau Beta Pi, Etta Kappa Nu, and Phi Kappa Phi.

**Roger L. King** (M'73–SM'95) received the B.S. degree from West Virginia University, Morgantown in 1973, the M.S. degree from the University of Pittsburgh, Pittsburgh, PA in 1978, both in electrical engineering, and the Ph.D. degree in engineering from the University of Wales–Cardiff, Cardiff, U.K., in 1988.

He began his career with Westinghouse Electric Corporation, but soon moved to the U.S. Bureau of Mines Pittsburgh Mining and Safety Research Center. Upon receiving his Ph.D. in 1988, he accepted a position in the Department of Electrical and Computer Engineering at Mississippi State University, where he now holds the position of Giles Distinguished Professor. At Mississippi State University, he is presently Associate Dean for Research and Graduate Studies in the Bagley College of Engineering.

Dr. King has received numerous awards for his research including the Department of Interior's Meritorious Service Medal. He is a Registered Professional Engineer in the State of Mississippi. Over the last 30 years, he has served in a variety of leadership roles with the IEEE Industry Applications Society, the Power Engineering Society, and the Geosciences and Remote Sensing Society (GRSS). He presently is a member of the IEEE GRSS AdCom.